Dor Gabay, Ali Yilmaz, Amir Boag, and Amir Natan

©SHUTTERSTOCK.COM/INFINITY32829

Modeling Electromagnetic Wave Phenomena in Large Quantum Systems

Formulation and computational costs.

The quantum framework of the time-dependent density functional theory (TDDFT) for analyzing nanostructured devices is reviewed, and alternative methods for incorporating induced electromagnetic fields into the theory are

discussed. To capture the retardation effects in larger electronic structures, the TDDFT equations can be formulated by applying the Lorenz gauge-fixing condition to the induced scalar and vector potentials (analogous to macroscopic formulations used in antenna theory). Evaluating the retarded potentials via radiation integrals, however, rapidly becomes the computational bottleneck within the TDDFT time-marching framework if done in

a brute-force manner. This article demonstrates that 3D space or 4D space–time fast Fourier transform (FFT) schemes can be adopted to accelerate these computations and reduce the costs of evaluating the potentials below the typical computational bottleneck of TDDFT. Thus, FFT-accelerated Lorenz gauge retarded potentials become an attractive candidate for replacing the conventionally used electrostatic-induced scalar potential within TDDFT.

INTRODUCTION

Constitutive equations are commonly used in electromagnetic engineering to model field–matter interactions, e.g., when designing antennas and other devices. As the device dimensions scale closer to the nanometer regime, constructing predictive models requires a quantum mechanical analysis of the interactions. The most rigorous approach to solving Schrödinger's equation is presently intractable as the many-body wave function of Schrödinger's equation dwells within a $4N_e + 1$ dimensional space (i.e., $3N_e$ spatial dimensions, N_e spin dimensions, and one temporal dimension) for an N_e particle system.

A more feasible and common approach in quantum mechanics is to resort to mean field approximations. The density functional theory (DFT) [1]–[4] and its time-dependent extension, the TDDFT [5]–[7], both of which are formulated in terms of the electron density rather than the many-body wave function, are such mean field approximations that can predictively model various physical properties of electronic structures.

DFT and TDDFT comprise a very successful and efficient theory for predicting material properties from quantum principles that presume nothing but the atomic structure. Properties such as the macroscopic dielectric function, phonon spectrum and infrared response, formation energies, and structure, among other observables, are all in excellent agreement with experiments [3], [4], [7], [8]. For large enough structures, one can use DFT and TDDFT or other mean field theories to calculate average macroscopic properties (e.g., the macroscopic dielectric response). These properties can then be transferred to classical electromagnetic simulations. For nanoscale structures, however, it is no longer possible to give a single macroscopic dielectric function; hence, there is a need to integrate electromagnetic field equations with the quantum calculations of DFT and TDDFT.

DFT maps the many-body Schrödinger equation to a set of single-particle equations, known as the Kohn–Sham equations, with the many electron interactions represented by an effective potential. This mapping was formulated by the Hohenberg–Kohn [1] and Kohn–Sham [2] theorems ([1] showed that the ground state total energy can be expressed as a function of the electron density, rather than the many-body wavefunction. Kohn's contributions to the development of DFT were recognized with the 1989 Nobel Prize in Chemistry). In doing so, DFT reduces the problem to a 3D space, simplifying the quantum mechanical analysis problem to a computationally tractable one. The resulting single-particle wave functions, henceforth referred to as *single-particle Kohn–Sham orbitals*,

are the eigenfunctions of the Kohn–Sham equation, which, for electrically small problems, involve a kinetic energy operator and an effective scalar potential. The effective scalar potential dictates the governing interactions of the single-particle orbitals, whereas the electron density, associated with the single-particle orbitals, predetermines the effective scalar potential, making it a highly nonlinear problem that can only be solved self-consistently. The solution of the Kohn–Sham equation provides the ground state of the electronic structure; this ground state solution is typically used as the initial condition within TDDFT, whereby the time-dependent single-particle orbitals are found by solving the equations via time marching.

Within the framework of DFT and TDDFT, electromagnetic interactions are formulated in terms of scalar and vector potentials rather than electric and magnetic fields. The inclusion of both vector and scalar potentials provides a much richer source of information in the context of quantum mechanics, as demonstrated by the Aharonov–Bohm effect [10], [11]. Unlike electric and magnetic fields, induced scalar and vector potentials directly couple to the phase of the complex single-particle orbitals. To adopt these potentials, a gauge-fixing condition must be prescribed.

Typically, the Coulomb gauge is adopted, and the associated retardation effects are ignored in the TDDFT formulations, i.e., only the induced scalar potential, which is solely dependent on the instantaneous frame of reference of the electron density, is considered, and the transverse contribution, attained via Helmholtz decomposition [12], is neglected as a result of ignoring the induced vector potential.

While this is appropriate when retardation effects are negligible, it does not suffice for larger electronic structures and higher than optical frequencies [13]; alternative gauges, such as the Lorenz gauge, which is used in this article, should be adopted. Evaluating retarded scalar and vector potentials that incorporate electromagnetic retardation effects via radiation integrals, however, increases the computational complexity of solving the TDDFT equations. This article demonstrates that these potentials can be rapidly evaluated by using FFT-based algorithms at a cost that no longer creates a bottleneck for the TDDFT calculations. As a result, the retarded potentials can be used in place of the conventional electrostatic-induced scalar potential at a marginal cost when studying retardation effects in large devices, such as nanoantennas [14], [15], and incorporating memory effects within the density-dependent effective potentials.

In this article, DFT and TDDFT are first briefly introduced. Thereafter, the Lorenz gauge-fixed time-dependent Kohn–Sham equation and a time-marching framework for solving it are presented. Next, the integral expressions for retarded potentials are discretized, and a 3D spatial FFT-based algorithm and a 4D space–time FFT-based algorithm for reducing the computational complexity are presented. Thereafter, numerical results that demonstrate the impact of the FFT-based acceleration are presented. Finally, the accelerated method is used to compute the temporal evolution of the electron density of a C_6H_4 model perturbed by a sine-squared laser pulse.

DFT AND TDDFT

A common approximation to the quantum modeling of matter is to treat the nuclei as point positive charges and the electrons as quantum mechanical objects interacting with electromagnetic fields. The many-electron Schrödinger's equation governs the electrons' evolution in time according to

$$i\frac{\partial}{\partial t}\Psi(\mathbf{x}_1,...,\mathbf{x}_{N_e},t) = \hat{\mathcal{H}}\Psi(\mathbf{x}_1,...,\mathbf{x}_{N_e},t), \quad (1)$$

where the many-electron wave function Ψ is defined in a $(4N_e+1)$-dimensional space, with $3N_e$ spatial dimensions, N_e discrete spin dimensions, and one temporal dimension, accounting for all possible interactions existing in a quantum mechanical system. Here, i is the imaginary unit, and $\hat{\mathcal{H}}$ is the Hamiltonian operator.

Here and throughout the text, atomic units (a.u.) [16] are adopted, whereby the reduced Planck constant, electron mass, and elementary charge are unity, i.e., $\hbar = m = e = 1$. The coordinate $\mathbf{x}$ is assumed to contain the spin, $\mathbf{x} = \{\mathbf{r}, \alpha\}$, where $\mathbf{r}$ and α are the spatial and spin coordinates, respectively. The spin coordinate is acted on by either spin-up or spin-down functions, which form an orthonormal basis.

The Pauli exclusion principle requires that the exchange of any two electron coordinates within the many-electron wave function results in a change of sign, i.e., $\Psi(\mathbf{x}_1,...,\mathbf{x}_n,...,\mathbf{x}_m,...,\mathbf{x}_{N_e}) = -\Psi(\mathbf{x}_1,...,\mathbf{x}_m,...,\mathbf{x}_n,...,\mathbf{x}_{N_e}) \,\forall n,m \in \{1,...,N_e\}$ and $n \neq m$. The Schrödinger Hamiltonian $\hat{\mathcal{H}}$ is composed of operators corresponding to the kinetic energy and effective potential energy acting on each of the particle's spatial coordinates. The effective potential is composed of an external perturbation and Coulomb interactions between all particle pairs. If the Hamiltonian operator of the system is not explicitly time dependent, it is possible to separate the time variable and get the time-independent Schrödinger equation by partitioning the temporal dependence from the many-electron wave function $\Psi(\mathbf{x}_1,...,\mathbf{x}_{N_e},t) \equiv \Psi_0(\mathbf{x}_1,...,\mathbf{x}_{N_e})e^{-iE_0t}$ and write

$$\hat{\mathcal{H}}\Psi_0(\mathbf{x}_1,...,\mathbf{x}_{N_e},t) = E_0\Psi_0(\mathbf{x}_1,...,\mathbf{x}_{N_e},t). \quad (2)$$

Here, E_0 is the ground state energy, which is the lowest eigenvalue of the Hamiltonian operator $\hat{\mathcal{H}}$. The resulting 3D electron density ϱ is given by

$$\varrho(\mathbf{r}) = N_e \int d\alpha \int d\mathbf{x}_2...d\mathbf{x}_{N_e} |\Psi_0(\mathbf{x},\mathbf{x}_2,...,\mathbf{x}_{N_e})|^2. \quad (3)$$

Here, the integral is taken over all of the other electron coordinates $\{\mathbf{x}_2,...,\mathbf{x}_{N_e}\}$ and the spin coordinate α of the first electron $\mathbf{x}$. The electron density (in our units, $e = 1$, equal to the charge density) defined by (3) represents the probability of seeing an electron at any given location. It is, hence, what is intuitively viewed as the electron cloud around the nuclei.

The direct solution of (1) is practically impossible because of the large number of degrees of freedom. To remedy this, mean field theories were developed to approximate the many-electron wave function and, in turn, alleviate the burden of dealing with a complex multidimensional problem. A key concept in attaining such mean field theories is the variational principle, which states that $\langle\Psi,\hat{\mathcal{H}}\Psi\rangle \geq E_0$ for any arbitrary normalized wave function [Here, the notation $\langle\Psi,\hat{\mathcal{H}}\Psi\rangle$ is simply the inner product.] Hence, the solution of (2) can be cast as a minimization problem, whereby the ground state wave function Ψ_0 is found by minimizing $\langle\Psi,\hat{\mathcal{H}}\Psi\rangle$ over all of the antisymmetric functions.

One of the first successful mean field approximations was that of Hartree–Fock (HF) [18]. In this approach, a Slater determinant [18] is used to characterize the antisymmetric property of the electron wave function and is hence a suitable ansatz for applying the variational principle. The resulting HF energy E_{HF} does not reach the true ground state energy E_0 of the many-body wave function. The energy difference $E_{HF} - E_0$ is commonly referred to as the correlation energy, which can be approximated by post-HF methods, e.g., [18]–[20].

Another successful mean field approach is DFT [21], [22], which utilizes a one-to-one mapping of the scalar potential to the electron density to variationally determine the total energy as a function of the density rather than the many-electron wave function, as justified by the Hohenberg–Kohn theorems [1]. By mapping the fully interacting system to a noninteracting one [2], the many-electron Schrödinger equation (2) is mapped to the single-electron many-orbitals Kohn–Sham equation

$$\hat{H}\psi_{n,\sigma}(\mathbf{r}) = \left[-\frac{1}{2}\nabla^2 + v_{s,\sigma}[\{\rho_\sigma\}](\mathbf{r})\right]\psi_{n,\sigma}(\mathbf{r}) = \epsilon_{n,\sigma}\psi_{n,\sigma}(\mathbf{r}), (4)$$

$$v_{s,\sigma}[\{\rho_\sigma\}](\mathbf{r}) = v_{\text{ind}}[\rho](\mathbf{r}) + v_{\text{ion}}[\rho](\mathbf{r}) + v_{xc,\sigma}[\{\rho_\sigma\}](\mathbf{r}). \quad (5)$$

Here, the Kohn–Sham Hamiltonian $\hat{H}$ contains both a kinetic energy contribution (represented by the Laplacian operator) and an effective scalar potential $v_{s,\sigma}$. The effective potential is composed of both classical phenomena, such as the induced v_{ind} and ionic v_{ion} potentials, as well as the many-body effects, like that of the exchange $v_{x,\sigma}$ and correlation $v_{c,\sigma}$ (i.e., where $v_{xc,\sigma} = v_{x,\sigma} + v_{c,\sigma}$).

Here, $\psi_{n,\sigma}$ is the nth electron orbital with a spin σ, which can be up ($\uparrow$) or down ($\downarrow$), and the eigenvalue $\epsilon_{n,\sigma}$ is the ground state energy of each such orbital. The electron density ρ, defined in (3) for the many-electron Schrödinger equation, and the electron density for a given spin orientation ρ_σ can be expressed in terms of the orbitals as

$$\rho(\mathbf{r}) = \rho_\uparrow(\mathbf{r}) + \rho_\downarrow(\mathbf{r}), \quad (6)$$

$$= \sum_{n=1}^{N_\uparrow} |\psi_{n,\uparrow}(\mathbf{r})|^2 + \sum_{n=1}^{N_\downarrow} |\psi_{n,\downarrow}(\mathbf{r})|^2, \quad (7)$$

where N_σ is the number of occupied orbitals for the spin σ.

For the sake of simplicity, a closed-shell configuration is assumed in the rest of this article, whereby $\psi_n(\mathbf{r}) \equiv \psi_{n,\uparrow}(\mathbf{r}) = \psi_{n,\downarrow}(\mathbf{r})$ and $N_o = N_\uparrow = N_\downarrow$ are the nth electron orbital and the number of orbitals, respectively. Furthermore, the energy eigenvalues in the Kohn–Sham equation are equal, $\epsilon_{n,\uparrow} = \epsilon_{n,\downarrow}$. In this configuration, the orbital $\psi_n(\mathbf{r})$ can be either doubly occupied with a pair of spin up and down

electrons or empty (thus, $N_e = 2N_o$), and the total magnetic spin of the system is zero. Therefore, in the following equations, the spin index is dropped, and the density is expressed as

$$\rho(\mathbf{r}) = 2 \sum_{n=1}^{N_o} |\psi_n(\mathbf{r})|^2. \tag{8}$$

The mapping by Kohn and Sham [2] is exact in theory but approximate in practice; there should be an exact v_{xc} that assures an exact mapping to (2), but it has not yet been found. Therefore, many approximations are used instead, e.g., the local density approximation and beyond [23], [24], to remedy the missing interactions in the noninteracting system. For a homogeneous electron gas, the Fock exchange interaction can be represented by the local Slater exchange [25], [26]. Both Slater and Dirac arrived at the same result for the local exchange using different arguments. As opposed to the HF method, DFT takes correlation energies into account. A major advantage of pure DFT methods is that both the exchange and correlation are expressed as local functionals of the density.

The induced scalar potential v_{ind} is commonly referred to as the Hartree potential and is the longitudinal component of the Coulomb gauge, attained via the Helmholtz decomposition [27]. It accounts for classical electrostatic fields and typically suffices for relatively small systems. Its differential and integral forms are as follows:

$$\nabla^2 v_{ind} = -4\pi\rho \ \rightleftharpoons \ v_{ind}(\mathbf{r}) = \int \frac{\rho(\mathbf{r}')}{|\mathbf{r} - \mathbf{r}'|} d\mathbf{r}'. \tag{9}$$

The ionic potential v_{ion} accounts for the electrostatic interaction of the electrons with the surrounding nuclei in much the same way.

The DFT equations are most commonly represented and solved in either the spectral or spatial basis. In the spectral representation, plane waves [28]–[30] are commonly utilized. In the spatial representation, either basis sets [31], wavelets [32], or real-space [33]–[35] methods are used. In this work, a real-space method, using high-order finite-difference equations on a spatially uniform grid, is used throughout. In the real-space method, it is trivial to split the domain/distribute the computation among processors, enabling the calculation of very large systems, such as silicon quantum dots [36], [37].

In similarly utilizing the Hohenberg–Kohn theorems along with an initial many-electron wave function Ψ_0, the Runge–Gross [5] theorem maps the time-dependent Schrödinger's equation (1) to a time-dependent Kohn–Sham equation using noninteracting time-dependent single-electron orbitals. The time-dependent version of DFT, known as TDDFT, determines the dynamical properties of a system in the presence of external perturbations. Formally, TDDFT is traditionally approached using one of two procedures: linear-response methods [38], [39] or real-time methods [7], [38], [40]–[42].

While linear-response methods result in the entire optical response spectrum with a reasonably low computational effort, real-time propagation schemes allow for the description of nonlinear effects such as high harmonics and ionization in the presence of strong lasers [43]–[47]. In this work, the real-time

method is adopted. In such an approach, the time-dependent Kohn–Sham equation and its corresponding effective potential take the form

$$i\frac{\partial}{\partial t}\psi_n(\mathbf{r},t) = \hat{H}\psi_n(\mathbf{r},t) = \left[-\frac{1}{2}\nabla^2 + v_s[\rho](\mathbf{r},t)\right]\psi_n(\mathbf{r},t), \tag{10}$$

$$v_s[\rho](\mathbf{r},t) = v_{ext}(\mathbf{r},t) + v_{ind}[\rho](\mathbf{r},t) + v_{ion}[\rho](\mathbf{r},t) + v_{xc}[\rho](\mathbf{r},t). \tag{11}$$

The time-dependent effective potential in (11) is composed of similar terms as that in (5) with the exception of the external potential v_{ext}. This term is used to perturb the specified initial single-particle orbitals, typically assumed to be the electronic structure's corresponding ground state. In the next section, magnetic fields are incorporated within this formal approach to account for the retardation effects; in the process, the Lorenz gauge-fixing condition is adopted.

OVERVIEW OF TDDFT IN THE LORENZ GAUGE

In solely adopting the electrostatic form of the induced scalar (Hartree) potential of (9), the transverse part of the Coulomb gauge (i.e., the vector potential) is effectively ignored. The Hartree potential is analogous to the longitudinal component of the electric field via Helmholtz decomposition and corresponds to null magnetic fields. Solely adopting the Hartree potential is satisfactory when the electronic structure of interest is significantly smaller than the wavelength of the external electromagnetic field, but it does not suffice for relatively large electronic structures or higher than optical frequencies. At these larger scales, retardation effects, which are not included in the instantaneous Hartree potential, begin to play an important role in characterizing the electron–electron interactions at long distances. Hence, either the full Coulomb gauge or the Lorenz gauge should be used.

To remedy this, the Lorenz gauge has been employed in TDDFT in an effort to incorporate induced electromagnetic fields in a more coherent manner [13], [49], [50]. (The formal proof of TDDFT presumes the Coulomb gauge-fixing condition, along with null magnetic fields. A fully gauge-invariant theory is achieved by TDCDFT. However, for weak enough magnetic fields, it is possible to include the full Coulomb or Lorenz gauges in TDDFT as an approximation to capture classical retardation effects in quantum systems. See [13] and references therein for a more detailed discussion.) The corresponding Kohn–Sham equation contains an additional effective vector potential within the Kohn-Sham Hamiltonian $\hat{H}$ (for $1 \le n \le N_o$):

$$i\frac{\partial}{\partial t}\psi_n(\mathbf{r},t) = \hat{H}\psi_n(\mathbf{r},t)$$
$$= \left[\frac{1}{2}\left(i\nabla + \frac{1}{c}A_s[j](r,t)\right)^2 + v_s[\rho](\mathbf{r},t)\right]\psi_n(\mathbf{r},t). \tag{12}$$

Here, c is the speed of light in free space, and the effective vector potential $\mathbf{A}_s$ contains both external $\mathbf{A}_{ext}$ and induced $\mathbf{A}_{ind}$ contributions:

$$\mathbf{A}_s[\mathbf{j}](\mathbf{r},t) = \mathbf{A}_{ext}(\mathbf{r},t) + \mathbf{A}_{ind}[\mathbf{j}](\mathbf{r},t). \tag{13}$$

The scalar and vector potentials are functionals of the time-dependent electron density ρ and total current density $\mathbf{j}$, which can be expressed as the composition of single-particle orbitals:

$$\rho(\mathbf{r},t) = 2 \sum_{n=1}^{N_o} \psi_n^*(\mathbf{r},t)\psi_n(\mathbf{r},t), \tag{14}$$

$$\mathbf{j}(\mathbf{r},t) = \sum_{n=1}^{N_o} i\left[\psi_n^*(\mathbf{r},t)\nabla\psi_n(\mathbf{r},t) - \psi_n(\mathbf{r},t)\nabla\psi_n^*(\mathbf{r},t)\right]$$
$$+ \frac{1}{c}\rho(\mathbf{r},t)\mathbf{A}_s(\mathbf{r},t). \tag{15}$$

The induced potentials, formulated via the Lorenz gauge [13], naturally contain retardation effects, which results in time delays of the form depicted in Figure 1. The governing integral expressions for these induced potentials are

$$v_{\text{ind}}(\mathbf{r},t) = \int \frac{\rho\left(\mathbf{r}',t - \frac{|\mathbf{r}-\mathbf{r}'|}{c}\right)}{|\mathbf{r}-\mathbf{r}|}d\mathbf{r}', \tag{16}$$

$$\mathbf{A}_{\text{ind}}(\mathbf{r},t) = \frac{1}{c}\int \frac{\mathbf{j}\left(\mathbf{r}',t - \frac{|\mathbf{r}-\mathbf{r}'|}{c}\right)}{|\mathbf{r}-\mathbf{r}'|}d\mathbf{r}'. \tag{17}$$

Evaluating the integral expressions of (16) and (17) is much more complicated than evaluating those of (9). Furthermore, doing so in a brute-force manner is expensive when compared to the other computational costs of solving the time-dependent Kohn–Sham equations, as detailed in the next section.

It is important to note that, in the previous formalism, the electronic system is treated quantum mechanically, but the field is treated with the semiclassical approximation. A fully quantum model would require one to quantize the electromagnetic field so as to incorporate spontaneous emission and absorption effects, particularly for systems perturbed at significantly higher energies than those considered in this work. This procedure has been achieved in the context of TDDFT by using a density-functional reformulation of the Pauli–Fierz Hamiltonian [51].

REAL-TIME, REAL-SPACE TDDFT

In this work, we use the Bayreuth version [42], [43] real-time propagation TDDFT code as part of the Pseudopotential Algorithm for Real-Space Electronic Structure Calculation (PARSEC) real-space package [33], [34] as a starting point for our code implementation. In the following, it is assumed that a grid of $N = N_x \times N_y \times N_z$ grid points is separated by $\Delta_x = \Delta_y = \Delta_z = h$ and that the single-particle Kohn–Sham orbitals are evolved by marching explicitly in time for N_t time samples at a time-step size Δt. The grid spacing depends on the electronic structure and typically ranges from 0.3 to 0.6 a.u. in the ground state and time-dependent calculations; the time-step size ranges from 0.5 to 1.5 attoseconds (as).

To march forward in time, a unitary evolution operator is applied to each of the single-particle Kohn–Sham orbitals. An explicit predictor–corrector scheme is used to assure sufficient accuracy of the single-particle orbitals and their associated densities. The predictor and corrector are characterized by a one-point integration method and an exponential midpoint formula, respectively [42]. The general procedure for each time step of a real-time predictor–corrector calculation is outlined in Figure 2. All of the potentials and densities attained by the predictor step are marked with an upperscore bar. The one-point integration method and midpoint rule can be applied to the unitary evolution operator to result in the following expressions (for $1 \leq n \leq N_o$):

$$\bar{\psi}_n(\mathbf{r},\ell\Delta t) = e^{-i\Delta t\hat{H}(\mathbf{r},(\ell-1)\Delta t)}\psi_n(\mathbf{r},(\ell-1)\Delta t), \tag{18}$$

$$\psi_n(\mathbf{r},\ell\Delta t) = e^{-i\Delta t\bar{\hat{H}}(\mathbf{r},(\ell-1/2)\Delta t)}\psi_n(\mathbf{r},(\ell-1)\Delta t). \tag{19}$$

Here, $\bar{\hat{H}}(\mathbf{r},(\ell-1/2)\Delta t)$ is attained by averaging $\hat{H}(\mathbf{r},(\ell-1)\Delta t)$ with $\hat{\bar{H}}(\mathbf{r},\ell\Delta t)$ using the orbitals $\bar{\psi}_n(\mathbf{r},\ell\Delta t)$. For numerical computations, the associated Taylor expansion of (18) and (19) (the "Predictor Step" and "Corrector Step" of Figure 2, respectively) is usually taken to order $N_\alpha = 4$ as

$$\bar{\psi}_n(\mathbf{r},\ell\Delta t) = \sum_{\alpha=0}^{N_\alpha} \frac{1}{\alpha!}\left[-i\Delta t\hat{H}(\mathbf{r},(\ell-1)\Delta t)\right]^\alpha \psi_n(\mathbf{r},(\ell-1)\Delta t), \tag{20}$$

$$\psi_n(\mathbf{r},\ell\Delta t) = \sum_{\alpha=0}^{N_\alpha} \frac{1}{\alpha!}\left[-i\Delta t\bar{\hat{H}}(\mathbf{r},(\ell-1/2)\Delta t)\right]^\alpha \psi_n(\mathbf{r},(\ell-1)\Delta t). \tag{21}$$

In addition to marching the single-particle orbitals in time, each time step requires evaluating the particle and current densities. While it is straightforward to compute the electron density of (14), evaluating the current density defined in (15) is more involved. Typically, the gradient of the complex single-particle orbitals is evaluated using high-order finite differences to reduce the error accumulation over many time steps. For example, using the sixth-order central difference, the x component of the gradient for the nth orbital is computed as

$$\frac{\partial\psi_n}{\partial x} \simeq \sum_{q=-6}^{6} \frac{c_q}{h}\psi_n(x_\kappa + qh, y_\kappa, z_\kappa, \ell\Delta t) \tag{22}$$

at each point $\mathbf{r}_\kappa = (x_\kappa, y_\kappa, z_\kappa)$ (for $1 \leq \kappa \leq N$). Here, q is an index running over the specified order of the differencing scheme, and c_q is the finite difference coefficient defined in [52]. Performing the differencing at each grid point $1 \leq \kappa \leq N$ requires $O(N)$ operations for each of the N_o single-particle orbitals.

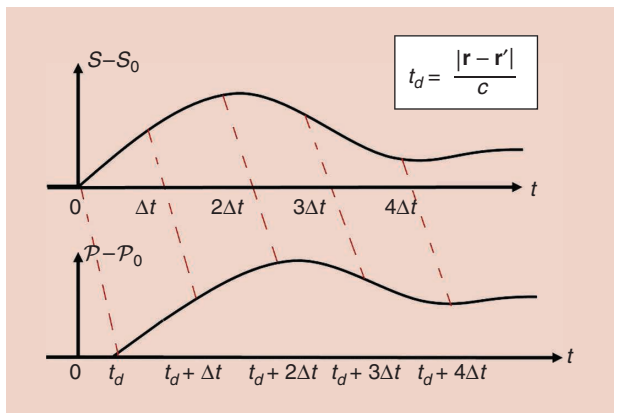The major computational costs of the real-time real-space TDDFT are as follows:

FIGURE 1. Retardation from the source density (e.g., $\mathcal{S} = \rho$) to the induced potential (e.g., $\mathcal{P} = v_{\text{ind}}$). The contribution $\mathcal{P}_0$ from the initial density $\mathcal{S}_0$ is computed separately.

1) *Predicting/correcting the single-particle orbitals:* The prediction/correction is performed using (20) and (21), which involves sparse matrix–vector multiplications that require $O(NN_o)$ operations per time step.
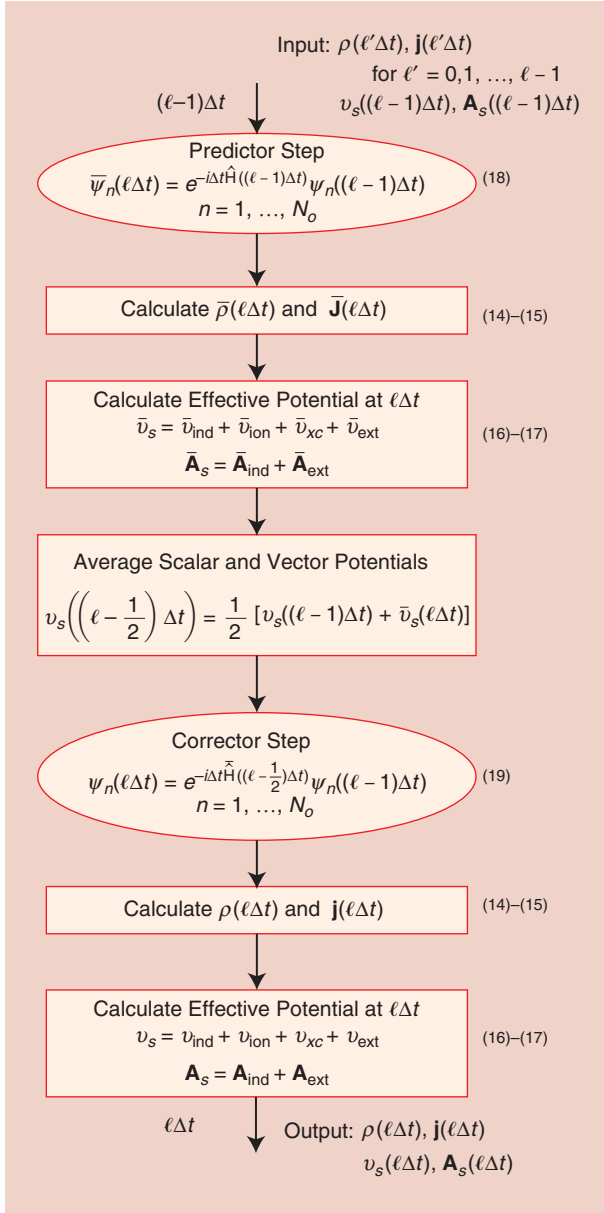

FIGURE 2. A depiction of the various operations within TDDFT occurring between time steps $(\ell-1)\Delta t$ and $\ell\Delta t$. All spatial dependencies on **r** are omitted for the purpose of clarity.
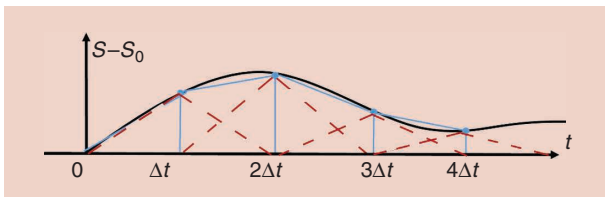

FIGURE 3. The red dashed lines represent the piecewise linear interpolatory temporal basis function.

2) *Calculating the current density:* Computing the current density of (15) involves higher-order finite differences that require $O(NN_o)$ operations.
3) *Evaluating retarded potential contributions:* Computing scalar/vector potential samples at all grid points using samples of particle/current densities at previous time steps requires $O(N^2)$ operations per time step, which is the main bottleneck for the TDDFT calculations that incorporate electromagnetic memory effects (typically, $N_o \ll N$) and must be accelerated to enable accurate characterization of large electronic structures.

A number of algorithms used in time-domain integral-equation solvers can be adopted to accelerate these retarded potential computations [53]–[56]; ideally, the costs of these computations should not exceed the $O(NN_o)$ cost of prediction/correction computations in (20) and (21). The following section describes an efficient procedure for rapidly evaluating these integral expressions via 3D and 4D FFTs that reduces the computational costs of the retarded potential evaluations below this level.

RETARDED POTENTIALS: DISCRETE FORM

The retarded potentials must be evaluated at each time step in propagating the Kohn–Sham orbitals. Let $\mathcal{S} \in \{\rho, \mathbf{j}\}$ denote the four-vector source density and $\mathcal{P} \in \{v_{\mathrm{ind}}, \mathbf{A}_{\mathrm{ind}}\}$ denote the corresponding four-vector induced potential. Then, the integral expressions in (16) and (17) can also be formulated as

$$\mathcal{P}(\mathbf{r}, t) = \int g_t(R, t) * \mathcal{S}(\mathbf{r}', t) d\mathbf{r}'$$
$$\approx \int G_t(R, t) * \mathcal{S}(\mathbf{r}', t) d\mathbf{r}'. \quad (23)$$

Here, the asterisk denotes temporal convolution; $R = |\mathbf{r} - \mathbf{r}'|$ is the distance; g_t is the time-domain Green's function,

$$g_t(R, t) = \frac{\delta\left(t - \frac{R}{c}\right)}{R}; \quad (24)$$

and the smoothed Green's function G_t is of the form

$$G_t(R, t) = \begin{cases} g_t(R, t) & R > d \\ G_{\mathrm{opt}}(R)\delta\left(t - \frac{R}{c}\right) & R \leq d, \end{cases} \quad (25)$$

where d is typically a distance of a few grid separations. In this article, the scalar Green's function's singular point, along with its near-singular points, is numerically optimized as detailed in [57] (i.e., formally known as the NOpt scalar Green's function kernel).

To compute the potentials, the sources, which are sampled in space–time using N grid points and N_t time samples, are interpolated in time. At each grid point $\kappa' = 1, \ldots, N$, the densities are approximated as

$$\mathcal{S}(\mathbf{r}_{\kappa'}, t) \simeq \mathcal{S}_0[\kappa'] + \sum_{l'=1}^{N_t} \mathcal{S}_{l'}[\kappa'] T(t - l'\Delta t), \quad (26)$$

where $\mathcal{S}_{l'}$ is a size N vector that stores the electron/current density samples at time $l'\Delta t$, and T is the temporal basis function [58], e.g., a piecewise linear interpolatory function depicted in Figure 3. In (26), $\mathcal{S}_0$ simply stores the initial densities associated with the ground state solution of (4).

By substituting (26) into (23), the potentials at grid point κ (for $1 \le \kappa \le N$) and time $l\Delta t$ (for $1 \le l \le N_t$) can be expressed as

$$\mathcal{P}(\mathbf{r}_\kappa, l\Delta t) \simeq \mathcal{P}_0[\kappa] + \sum_{\kappa'=1}^{N} G_0[\kappa, \kappa'] \mathcal{S}_l[\kappa']$$
$$+ \sum_{l'=\max(1,l-N_g)}^{l-1} \sum_{\kappa'=1}^{N} G_{l-l'}[\kappa, \kappa'] \mathcal{S}_{l'}[\kappa'], \quad (27)$$

where $\mathcal{P}_0$ is the electrostatic potential associated with the ground state density $\mathcal{S}_0$, and $N_g = \mathcal{D}/c\Delta t$ is the number of time steps needed to propagate over distance $\mathcal{D}$, the maximum separation between any two points on the grid. Each propagation matrix $\mathbf{G}_{l-l'}$ is an $N \times N$ matrix that relates the sources at time $l'\Delta t$ to potentials at time $l\Delta t$:

$$G_{l-l'}[\kappa, \kappa'] = G_t(|\mathbf{r}_\kappa - \mathbf{r}_{\kappa'}|, t) * T(t - l'\Delta t)|_{t=l\Delta t}. \quad (28)$$

Each $G_{l-l'}$ matrix has a three-level block Toeplitz structure as a result of the space–time translational invariance of the Green's function and the uniform sampling.

Notice that the contribution from sources at the same time step as the observer ($l' = l$) is separated from the other contributions in (27). This is because the predictor–corrector scheme depicted in Figure 2 requires the computation of the potentials once with the predicted and once with the corrected charge/current density samples at the concurrent time $l\Delta t$. By storing the contributions from sources at all of the other time steps to avoid their recomputation and by computing only the same-time-step contributions twice (once with the predicted samples and once with the corrected ones), the computational cost can be reduced by a factor of ~2. Nevertheless, directly computing the multiplications in (27) remains expensive as it requires $O(N^2)$ operations.

The computational costs of the brute-force approach can be alleviated by using 3D spatial FFTs to convert the spatial convolutions on the right-hand side of (27) to multiplications (for $1 \le \kappa \le 8N$):

$$\tilde{\mathcal{P}}_0[\kappa] + \tilde{G}_0[\kappa]\tilde{\mathcal{S}}_l[\kappa] + \sum_{l'=\max(1,l-N_g)}^{l} \tilde{G}_{l-l'}[\kappa]\tilde{\mathcal{S}}_{l'}[\kappa]. \quad (29)$$

Here, $\tilde{\mathcal{P}}_0$, $\tilde{\mathcal{S}}$, and $\tilde{G}$ are discrete Fourier transforms of $\mathcal{P}_0$, $\mathcal{S}$, and G, respectively, computed using 3D FFTs with appropriate zero padding (doubling in each grid dimension to a 3D FFT size of 8 N) to ensure open (rather than periodic) boundary conditions [9], [17], [48], [53], [59]. This reduces the computational cost to $O(N_g N + N \log N)$ operations per time step, which is sufficient for handling small molecules and molecular chains with lengths reaching up to a few nanometers.

Larger electronic structures require more advanced methods, such as those applying FFT procedures in not just space but also time. For example, the multiplication in (27) can be efficiently computed by using blocked 4D space–time FFTs while marching in time according to the recipe in [9], [17], and [48]. The blue boxes in Figure 4 illustrate the structure of these blocks; at each time step, only one such block is multiplied to compute the partial contributions from sources at previous time steps to the potentials at the current and future time steps.

In the 4D FFT approach, at each time step, one 3D forward spatial FFT of size $8N$; one 3D inverse spatial FFT of size 8 N; 8 N temporal 1D forward and inverse FFTs, whose size varies depending on the time step; and 8 N element-by-element multiplications are performed to evaluate the samples of each retarded potential. Figure 4 also depicts the separation of contributions from sources at the previous and current time step; this separation is critical to properly accelerate the computations within the predictor–corrector scheme. Using this approach, the induced potentials can be evaluated in a total of $\mathcal{O}(N[\log N + \log^2 N_g])$ operations per time step [9], [17], [48].
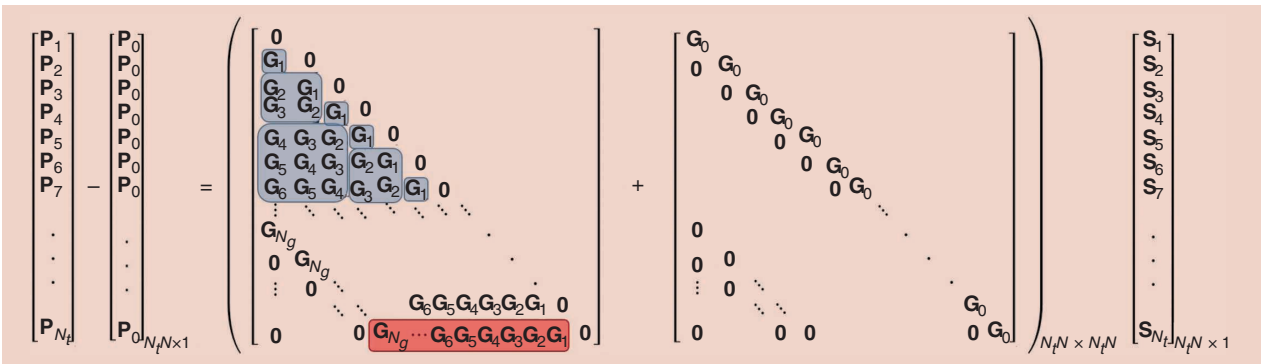

FIGURE 4. Two possible ways of rapidly evaluating the matrix–vector products while marching in time. First, the 3D FFT approach, where, at each time step, P_l is attained by multiplying the past densities ($S_{l-N_g}, ..., S_{l-1}$) with the corresponding matrix blocks ($G_{N_g}, ..., G_1$) using 3D spatial FFTs. For illustration, this is shown for P_{N_t} in the red box of the last row of the matrix. For $l < N_g$, fewer than N_g elements would have to be evaluated. Second, the 4D FFT approach, where, at each time step, we multiply portions of the past densities with the corresponding matrix blocks (shown in blue boxes) using 4D space–time FFTs. In this approach, the full potential at the current time step and partial potentials at future time steps are computed. In both approaches, contributions from sources at the current time step to the potential P_l are found by multiplying $\mathbf{G}_0$ first with $\bar{S}_l$ and then with S_l according to the predictor–corrector scheme. We demonstrate the difference between the two approaches by looking at row 7 and assuming $N_g \ge 6$. In the 3D FFT approach, the value of P_7 is computed by a direct sum, $P_7 = \sum_{i=0}^{6} G_{6-i} \cdot S_{i+1}$. In the 4D FFT approach, there are already partial results from the 3×3 box ($G_6 \cdot S_1 + G_5 \cdot S_2 + G_4 \cdot S_3$) calculated in row 5 and the 2×2 box ($G_3 \cdot S_4 + G_2 \cdot S_5$) calculated in row 6. We therefore need only to evaluate $G_1 \cdot S_6 + G_0 \cdot S_7$ to ascertain P_7.

INCORPORATING MEMORY EFFECTS

This section demonstrates how the 3D and 4D FFT-based acceleration algorithms enable the incorporation of electromagnetic memory effects of (16) and (17) within the Kohn–Sham equation (12) in a computationally affordable manner. As detailed in the "Real-Time, Real-Space TDDFT" section, the brute-force direct calculation of potentials has a computational cost that is beyond that of the typically accepted $O(NN_o)$ operations necessary for predicting/correcting orbitals in TDDFT. Indeed, it is necessary to reduce the cost of evaluating potentials below this computational cost to be able to explore dynamical systems without being limited to the sole use of the electrostatic-induced scalar potential.

In the following analysis, the cumulene structure $H_2(=C_6=)H_2$ is adopted to profile the various computational costs. The 1D carbon chain is placed along the z-axis, and its hydrogen atoms are placed along the yz plane. The C–C and H–H bond lengths are 2.39 and 2.07 a.u., respectively. The cumulene's cross section is fixed to a relatively small size of $N_x = 15$, $N_y = 15$, while its z-axis is varied from $N_z = 20$ to 500. Increasing the size of the grid along the z-axis serves as a numerical tool to measure the computational cost of incorporating more retardation effects. The electronic structure was chosen to have a grid spacing of $h = 0.5$ a.u. and a time step of $\Delta t = 0.5$ as. The resulting number of saved past densities varies from $N_g = 5$ to 88. The number of orbitals used was $N_o = 16$. The chosen parameters are not optimal; rather, they serve as a way of studying the computational cost of the proposed methodologies. For more realistic parameter settings of electronic structures of the form C_{N_a} (N_a – number of atoms), see [13].

The chosen cumulene structure is significantly smaller than the external electromagnetic field's wavelength; hence, the aforementioned retardation effects are negligible, and the electronic structure can be sufficiently characterized using the traditional formulation of TDDFT. In previous work [13], we showed that for such small structures, our implementation of the Lorenz and full Coulomb gauges give the same results as the traditional length gauge, which does not include retardation effects. Studying such effects requires longer carbon chains of more than 600–800 atoms (around 75–100 nm), which is still a
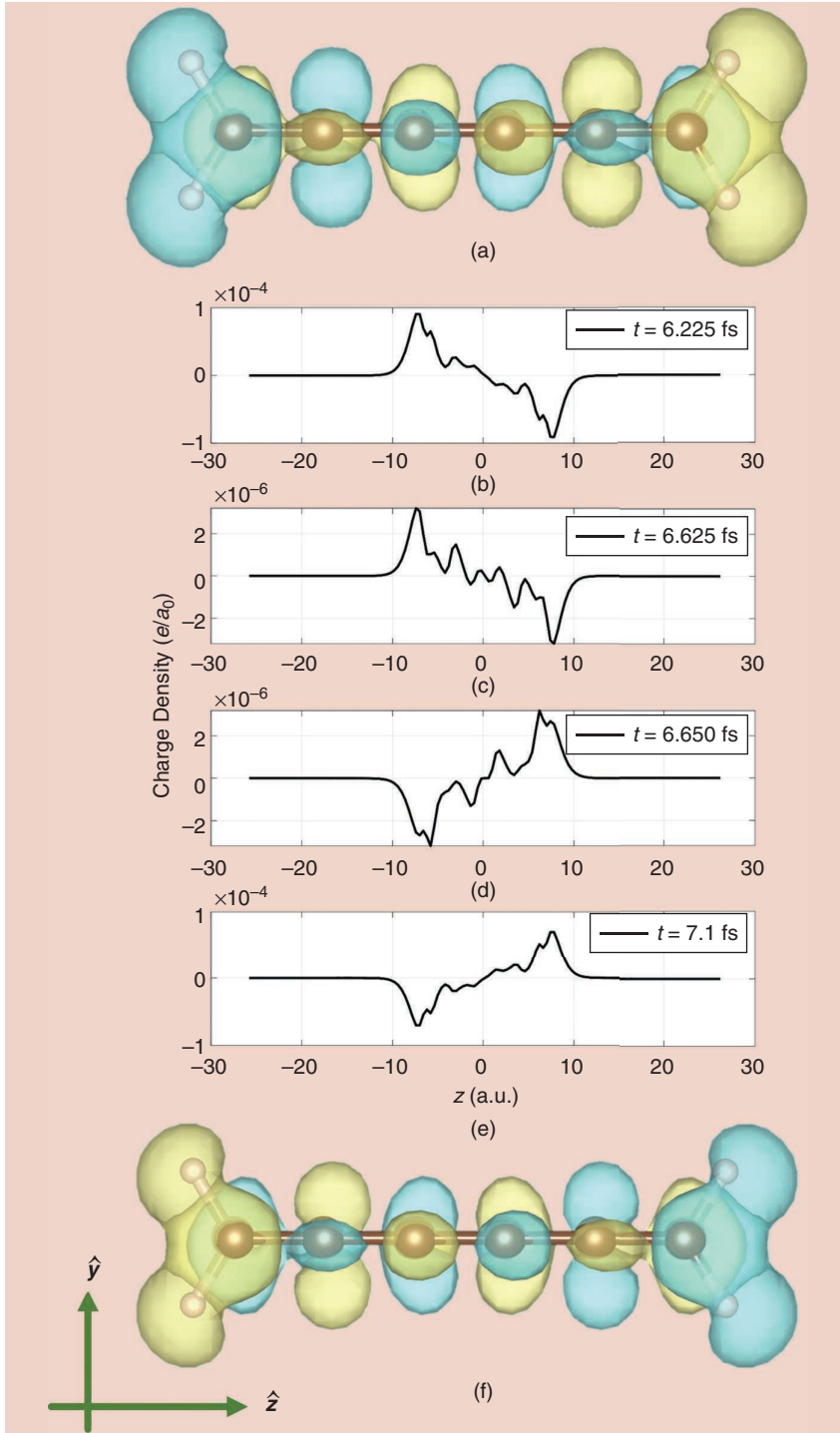

FIGURE 5. The yellow and blue colors indicate the positive and negative parts, respectively, of the difference in the electron density for the C_6H_4 molecular structure at time t from its ground state solution $\rho(t) - \rho(0)$. (a) The C_6H_4 molecular structure and charge density difference at time $t = 6.225$ fs; in (b)–(e), the charge density is averaged over the xy plane at every point z, resulting in plots at (b) time sample $t = 6.225$ fs; (c) time sample $t = 6.625$ fs; (d) time sample $t = 6.650$ fs; (e) time sample $t = 7.100$ fs; and (f) the C_6H_4 molecular structure and charge density difference at time $t = 7.100$ fs.

computational challenge. In this work, we analyzed C_6H_4 to identify the numerical properties of the proposed FFT algorithm, which is a crucial step in eventually reaching such length scales.

To exemplify the resulting dynamics of the electronic structure, C_6H_4 (with $N_z = 114$ and $N_g = 22$) is perturbed by a sine-squared pulse for a 10-femtoseconds (fs) duration. More specifically, a linearly polarized external electromagnetic field is applied along the $\hat{z}$-direction, and its corresponding electric field varies along the x-axis as

$$\mathbf{E}_{\text{ext}}(x,t) = A_s \sin^2 \left[\omega_{\text{env}} t - \frac{\omega_{\text{env}}}{c} x \right] \sin \left[\omega t - \frac{\omega}{c} x \right] \hat{z}. \quad (30)$$

Here, $A_s = 6 \times 10^{12}$ W/m^2, $\omega = 23.5$ rad·s^{-1} (corresponding to 800 nm), and $\omega_{\text{env}} \approx 5\omega$ are the intensity, radial frequency, and radial envelope frequency, respectively. Absorbing boundary conditions, with a boundary layer of 5 a.u. on each side, are used to mitigate any reflections from the boundary. Two time samples of the electron density are displayed in Figure 5, each depicting the difference in electron density from a given time t to its initial ground state (i.e., initial condition): $\rho(t) - \rho(0)$. Figure 5(a) ($t = 6.225$ fs) is dominantly positive (blue), while Figure 5(f) ($t = 7.100$ fs) is dominantly negative (yellow) on the left side of the C_6H_4 molecular structures. The particle difference is antisymmetric, resulting in a dipole moment that fluctuates as depicted in Figure 5(b)–(e) for various times. At $t = 0.0$ and 10.0 fs, the dipole moments cease to exist.

Next, the computational costs of various steps depicted in Figure 2 are measured to determine whether the accelerated retarded potential computations remain the computational bottleneck of TDDFT.

THE BRUTE-FORCE APPROACH
In TDDFT calculations, the major components of the total computational time can be classified as
1) the unitary evolution operator of the single-particle Kohn–Sham orbitals in (20) and (21)
2) evaluation of the current density $\mathbf{j}$ in (15)
3) determination of the electrostatic induced scalar potential of (9) or induced retarded potentials of (16) and (17)
4) the calculation of the ionic potential v_{ion}
5) the evaluation of the exchange-correlation scalar potential v_{xc}.

As described in the "Real-Time, Real-Space TDDFT" section, for real-time TDDFT calculations that do not incorporate electromagnetic retardation effects, component 1 serves as the major bottleneck, requiring $O(NN_o)$ operations. Component 3 typically follows, with the number of operations depending on the algorithm of choice. The current density and ionic potential computations in components 2 and 4 require that gradient operations be applied on each of the single-particle orbitals, but they are significantly less expensive than the unitary evolution operator. Finally, local exchange-correlation potentials in component 5 are usually fairly simple to evaluate, requiring no more than $O(N)$ operations. Any other calculations required can be deemed either trivial or not a necessity. In the following analysis, the computational complexity of components 4 and 5 are not presented since 6 is of the same computational complexity as 2, while 5 is fairly negligible for local density approximations.

As can be seen in Figure 6, the cost of the brute-force calculation of the retarded potentials dominates that of the unitary evolution operation, the typical TDDFT bottleneck. Each point in the figure represents the average computational time of any given task over the course of a 20-as simulation time. This clearly poses a problem in attempting to affordably incorporate electromagnetic retardation effects. The time needed to compute the Hartree potential v_H (using a 3D FFT procedure) sits well below that required for the unitary evolution, while the time needed to compute the total current density $\mathbf{j}$ sits somewhere in between.

BYPASSING THE BOTTLENECK
Figure 7 compares the computational cost of the 3D and 4D FFT acceleration schemes to the previously explored computational tasks. Each point in the figure represents the average computational time of any given task over the course of a 20-as simulation time. As can be seen in Figure 7, the 3D FFT algorithm is quite efficient at smaller length scales but inevitably surpasses the $O(NN_o)$ bottleneck for values of $N_g > N_o$. On the other hand, it can typically be assumed that $\log^2 N_g \ll N_o$, even for the worst-case scenario of an elongated structure with large N_g and relatively small N_o. The 4D FFT scheme, therefore, appears to be necessary for structures with a large N_g/N_o ratio; otherwise, the 3D FFT scheme suffices.

It should be noted that the elongated electronic structure studied here corresponds to the most expensive scenario for 3D and 4D FFT-based acceleration of retarded potential calculations. This is because the grid size, time step, and number of
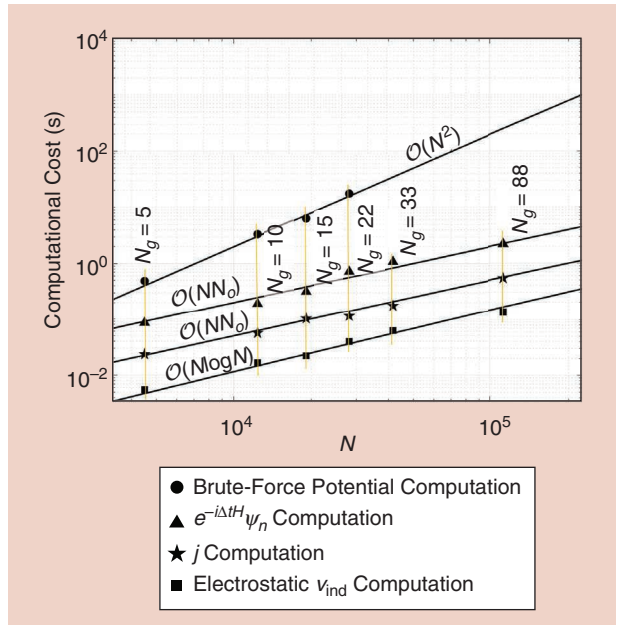

FIGURE 6. The average time required at each time step for computing the electrostatic-induced scalar (Hartree) potential (squares), current density (stars), and unitary evolution operator (triangles) and evaluating the retarded potentials directly (circles). The brute-force evaluation of the retarded potentials dominates all of the other computational costs.
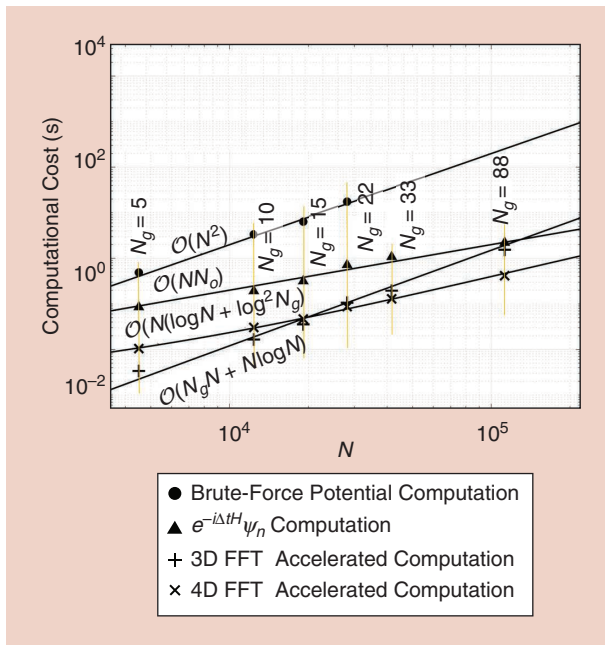
FIGURE 7. The average time required at each time step to evaluate the retarded potentials using the brute force (circles), unitary evolution operator (triangles), 3D FFT (plus signs), and 4D FFT (x marks) approaches. The costs of both the 3D and 4D FFT acceleration schemes remain below the cost of the unitary evaluation operator until N_g surpasses the number of orbitals N_o, when the 4D FFT scheme becomes necessary.

orbitals result in a rapidly growing N_g for increasing N, such that $N_g \gg N_o$. This typically occurs only in elongated structures, such as C_6H_4. For structures that are not elongated, the number of Kohn–Sham orbitals N_o, which scales proportionally to the volume, would be significantly larger than the saved past time steps N_g, which scales proportionally to the maximum length of the grid, implying that the cost of computing the retarded potentials with 3D or 4D FFTs would be even smaller than that of the unitary evolution operator for nonelongated electronic structures.

CONCLUSIONS

In TDDFT simulations that include electromagnetic retardation effects, the calculation of retarded potentials is significantly slower than that of the Hartree potential. The proposed algorithms reduce their costs well under the typical $O(NN_o)$ operations needed for the unitary evolution operation—the typical TDDFT bottleneck. Indeed, the computational inefficiency of the brute-force scheme for incorporating electromagnetic memory effects via retarded potentials can be effectively averted by invoking 3D and 4D FFT operations onto the retarded integral expressions. The 4D FFT scheme was shown to be necessary for electronic structures with large N_g/N_o ratios. Otherwise, for most structures, the 3D FFT scheme should suffice.

The required level of approximation for modeling electronic structures depends on the system size, geometry, and composition. Clearly, large enough systems can be successfully modeled by fully classical methods, while small molecules, up to a few nanometers in size, should be modeled by quantum mechanical methods and do not have significant retardation effects. For slightly larger systems (tens or hundreds of nanometers in size), quantum effects are still important, but classical retardation effects might appear.

Therefore, by enhancing quantum computational methods, we hope that it will be possible to compute systems large enough to identify the length scales whereby retardation effects are critical. Further scaling up will allow us to identify the regime where mean field macroscopic modeling of the system suffices (i.e., fully classical electromagnetic simulations). With the methods described in this article, we were able to model elongated systems of up to 5 nm [13]. The advent of faster time propagation methods and additional parallelization schemes will enable the study of elongated structures with significant retardation effects, reaching lengths of 100–200 nm. Such an elongated structure may be long in one dimension but only a few nanometers in its cross sections, thus requiring quantum treatment.

AUTHOR INFORMATION

Dor Gabay (dor0gabay@gmail.com) received his Ph.D. degree in electrical engineering from Tel Aviv University under the supervision of Prof. Amir Boag and Dr. Amir Natan. His current research interests include topological states of matter and their implication for topological quantum computing.

Ali Yilmaz (ayilmaz@mail.utexas.edu) is with the Institute for Computational Engineering and Sciences, University of Texas at Austin, Austin, Texas, 78712, USA. He is a Senior Member of IEEE.

Amir Boag (boag@eng.tau.ac.il) is with the Department of Physical Electronics, Tel Aviv University, Tel Aviv, 69978, Israel. He is a Fellow of IEEE.

Amir Natan (amirnatan@post.tau.ac.il) is with the Department of Physical Electronics and the Sackler Center for Computational Molecular and Materials Science, Tel Aviv University, Tel Aviv, 69978, Israel.

REFERENCES

[1] P. Hohenberg and W. Kohn, "Inhomogeneous electron gas," *Phys. Rev.*, vol. 136, no. 3B, p. B864, 1964. doi: 10.1103/PhysRev.136.B864.
[2] W. Kohn and L. J. Sham, "Self-consistent equations including exchange and correlation effects," *Phys. Rev.*, vol. 140, no. 4A, p. A1133, 1965. doi: 10.1103/PhysRev.140.A1133.
[3] W. Koch and M. C. Holthausen, *A Chemist's Guide to Density Functional Theory*. Hoboken, NJ: Wiley, 2015.
[4] R. G. Parr and Y. Weitao, *Density Functional Theory of Atoms and Molecules*. London, U.K.: Oxford Univ. Press, 1994.
[5] E. Runge and E. K. U. Gross, "Density-functional theory for time-dependent systems," *Phys. Rev. Lett.*, vol. 52, no. 12, p. 997, 1984. doi: 10.1103/PhysRevLett.52.997.
[6] M. E. Casida and M. Huix-Rotllant, "Progress in time-dependent density-functional theory," *Annu. Rev. Phys. Chem.*, vol. 63, no. 1, pp. 287–323, 2012. doi: 10.1146/annurev-physchem-032511-143803.
[7] C. A. Ullrich, *Time-Dependent Density-Functional Theory: Concepts and Applications*. London, U.K.: Oxford Univ. Press, 2011.
[8] R. M. Martin, *Electronic Structure: Basic Theory and Practical Methods*. Cambridge, U.K.: Cambridge Univ. Press, 2004.
[9] A. E. Yilmaz, J.-M. Jin, and E. Michielssen, "Time domain adaptive integral method for surface integral equations," *IEEE Trans. Antennas Propag.*, vol. 52, no. 10, pp. 2692–2708, 2004. doi: 10.1109/TAP.2004.834399.
[10] Y. Aharonov and D. Bohm, "Significance of electromagnetic potentials in the quantum theory," *Phys. Rev.*, vol. 115, no. 3, p. 485, 1959. doi: 10.1103/PhysRev.115.485.
[11] L. Vaidman, "Role of potentials in the Aharonov-Bohm effect," *Phys. Rev. A*, vol. 86, no. 4, p. 040101, 2012. doi: 10.1103/PhysRevA.86.040101.
[12] O. L. Brill and B. Goodman, "Causality in the Coulomb gauge," *Am. J. Phys.*, vol. 35, no. 9, pp. 832–837, 1967. doi: 10.1119/1.1974261.

[13] D. Gabay, A. Yilmaz, V. Lomakin, A. Boag, and A. Natan, "Lorenz gauge formulation for time-dependent density functional theory," *Phys. Rev. B*, vol. 101, no. 23, p. 235,101, 2020. doi: 10.1103/PhysRevB.101.235101.

[14] G. Slepyan, T. Gilad, and A. Boag, "Quantum light rectification in nano-rectennas," in *Proc. 2017 IEEE Int. Symp. Antennas Propag. & USNC/URSI Nat. Radio Sci. Meeting*, pp. 1051–1052.

[15] E. Donchev et al., "The rectenna device: From theory to practice (a review)," *MRS Energy Sustain.*, vol. 1, pp. 1–34, July 2014. doi: 10.1557/mre.2014.10.

[16] B. W. Petley, "The atomic units, the kilogram and the other proposed changes to the SI," *Metrologia*, vol. 44, no. 1, p. 69, 2007. doi: 10.1088/0026-1394/44/1/010.

[17] E. Hairer, C. H. Lubich, and M. Schlichte, "Fast numerical solution of non-linear Volterra convolution equations," *SIAM J. Sci. Stat. Comput.*, vol. 6, no. 3, pp. 532–541, 1985. doi: 10.1137/0906037.

[18] A. Szabo and N. S. Ostlund, *Modern Quantum Chemistry: Introduction to Advanced Electronic Structure Theory*. North Chelmsford, MA: Courier Corporation, 2012.

[19] C. Møller and M. S. Plesset, "Note on an approximation treatment for many-electron systems," *Phys. Rev.*, vol. 46, no. 7, pp. 618–622, 1934. doi: 10.1103/PhysRev.46.618.

[20] J. Cizek, "On the correlation problem in atomic and molecular systems. Calculation of wavefunction components in Urselltype expansion using quantumfield theoretical methods," *J. Chem. Phys.*, vol. 45, no. 11, pp. 4256–4266, 1966. doi: 10.1063/1.1727484.

[21] K. Burke, "Perspective on density functional theory," *J Chem. Phys.*, vol. 136, no. 15, p. 150,901, 2012. doi: 10.1063/1.4704546.

[22] E. Engel and R. M. Dreizler, *Density Functional Theory*. Berlin: Springer-Verlag, 2011.

[23] A. D. Becke, "Density functional theories in quantum chemistry: Beyond the local density approximation," in *The Challenge of d and f Electrons: Theory and Computation*, D. R. Salahub and M. C. Zerner, Eds. Washington, D.C.: American Chemical Society, 1989, pp. 165–179.

[24] D. C. Langreth and M. J. Mehl, "Beyond the local-density approximation in calculations of ground-state electronic properties," *Phys. Rev. B*, vol. 28, no. 4, p. 1809, 1983. doi: 10.1103/PhysRevB.28.1809.

[25] P. A. M. Dirac, "Note on exchange phenomena in the Thomas atom," *Math. Proc. Camb. Philos. Soc.*, vol. 26, no. 3, pp. 376–385, 1930. doi: 10.1017/S0305004100016108.

[26] J. C. Slater, "A simplification of the Hartree-Fock method," *Phys. Rev.*, vol. 81, no. 3, p. 385, 1951. doi: 10.1103/PhysRev.81.385.

[27] J. D. Jackson, "From Lorenz to Coulomb and other explicit gauge transformations," *Am. J. Phys.*, vol. 70, no. 9, pp. 917–928, 2002. doi: 10.1119/1.1491265.

[28] J. Ihm, A. Zunger, and M. L. Cohen, "Momentum-space formalism for the total energy of solids," *J. Phys. C*, vol. 12, no. 21, p. 4409, 1979. doi: 10.1088/0022-3719/12/21/009.

[29] G. Sun, J. Kurti, P. Rajczy, M. Kertesz, J. Hafner, and G. Kresse, "Performance of the Vienna ab initio simulation package (VASP) in chemical applications," *J. Mol. Struct.: THEOCHEM*, vol. 624, nos. 1–3, pp. 37–45, 2003. doi: 10.1016/S0166-1280(02)00733-9.

[30] P. Giannozzi et al., "QUANTUM ESPRESSO: A modular and open-source software project for quantum simulations of materials," *J. Phys., Condens. Matter.*, vol. 21, no. 39, p. 395,502, 2009.

[31] E. R. Davidson and D. Feller, "Basis set selection for molecular calculations," *Chem. Rev.*, vol. 86, no. 4, pp. 681–696, 1986. doi: 10.1021/cr00074a002.

[32] T. Torsti et al., "Three realspace discretization techniques in electronic structure calculations," *Phys. Stat. Solidi B*, vol. 243, no. 5, pp. 1016–1053, 2006. doi: 10.1002/pssb.200541348.

[33] J. R. Chelikowsky, N. Troullier, K. Wu, and Y. Saad, "Higher-order finite-difference pseudopotential method: An application to diatomic molecules," *Phys. Rev. B*, vol. 50, no. 16, p. 11,355, 1994. doi: 10.1103/PhysRevB.50.11355.

[34] L. Kronik et al., "PARSEC–The pseudopotential algorithm for realspace electronic structure calculations: Recent advances and novel applications to nanostructures," *Phys. Stat. Solidi. B*, vol. 243, no. 5, p. 1063, 2006. doi: 10.1002/pssb.200541463.

[35] A. Castro et al., "Octopus: A tool for the application of time-dependent density functional theory," *Phys. Stat. Solidi B*, vol. 243, no. 11, pp. 2465–2488, 2006. doi: 10.1002/pssb.200642067.

[36] J. R. Chelikowsky, M. L. Tiago, Y. Saad, and Y. Zhou, "Algorithms for the evolution of electronic properties in nanocrystals," *Comput. Phys. Commun.*, vol. 177, nos. 1–2, pp. 1–5, 2007. doi: 10.1016/j.cpc.2007.02.072.

[37] D. Gabay, X. Wang, V. Lomakin, A. Boag, M. Jain, and A. Natan, "Size dependent electronic properties of silicon quantum dots: An analysis with hybrid, screened hybrid and local density functional theory," *Comput. Phys. Commun.*, vol. 221, pp. 95–101, 2017. doi: 10.1016/j.cpc.2017.08.005.

[38] M. A. L. Marques, N. T. Maitra, F. M. S. Nogueira, E. K. U. Gross, and A. Rubio, *Fundamentals of Time-Dependent Density Functional Theory*, vol. 837, Berlin: Springer-Verlag, 2012.

[39] M. E. Casida, "Time-dependent density functional response theory for molecules," in *Proc. Recent Adv. Density Funct. Methods, (Part I)*, 1995, pp. 155–192. doi: 10.1142/9789812830586_0005.

[40] A. Castro, M. A. L. Marques, J. A. Alonso, G. F. Bertsch, and A. Rubio, "Excited states dynamics in time-dependent density functional theory," *Eur. Phys. J. D-Atomic, Molecular, Opt. Plasma Phys.*, vol. 28, no. 2, pp. 211–218, 2004. doi: 10.1140/epjd/e2003-00306-3.

[41] A. G. Pueyo, M. A. L. Marques, A. Rubio, and A. Castro, "Propagators for the time-dependent Kohn-Sham equations: Multistep, Runge-Kutta, Exponential Runge-Kutta, and Commutator free magnus methods," *J. Chem. Theory Comput.*, vol. 14, no. 6, pp. 3040–3052, 2018. doi: 10.1021/acs.jctc.8b00197.

[42] M. Mundt, "Real-time approach to time-dependent density-functional theory in the linear and nonlinear regime," *J. Theor. Comput. Chem.*, vol. 8, no. 4, pp. 561–574, 2004. doi: 10.1142/S0219633609004915.

[43] M. Mundt and S. Kummel, "Photoelectron spectra of anionic sodium clusters from time-dependent density-functional theory in real time," *Phys. Rev. B*, vol. 76, no. 3, p. 035413, 2007. doi: 10.1103/PhysRevB.76.035413.

[44] S. K. Son and S. I. Chu, "Multielectron effects on the orientation dependence and photoelectron angular distribution of multiphoton ionization of CO_2 in strong laser fields," *Phys. Rev. A*, vol. 80, no. 1, p. 011403, 2009.

[45] D. A. Telnov and S. I. Chu, "Effects of multiple electronic shells on strong-field multiphoton ionization and high-order harmonic generation of diatomic molecules with arbitrary orientation: An all-electron time-dependent density-functional approach," *Phys. Rev. A*, vol. 80, no. 4, p. 043412, 2009. doi: 10.1103/PhysRevA.80.043412.

[46] E. Yahel and A. Natan, "Effect of multiorbital contributions to strong-field ionization of benzene derivatives," *Phys. Rev. A*, vol. 98, no. 5, p. 053421, 2018. doi: 10.1103/PhysRevA.98.053421.

[47] I. Flosse et al., "Ab initio multiscale simulation of high-order harmonic generation in solids," *Phys. Rev. A*, vol. 97, no. 1, p. 011401, 2018. doi: 10.1103/PhysRevA.97.011401.

[48] A. E. Yilmaz, D. S. Weile, B. Shanker, J.-M. Jin, and E. Michielssen, "Fast analysis of transient scattering in lossy media," *IEEE Antennas Wireless Propag. Lett.*, vol. 1, pp. 14–17, 2002. doi: 10.1109/LAWP.2002.802577.

[49] D. Gabay, A. E. Yilmaz, A. Boag, and A. Natan, "Fast evaluation of retarded electromagnetic potentials for quantum calculations," in *Proc. 2019 IEEE Int. Symp. Antennas Propag. USNC-URSI Radio Sci. Meeting*, pp. 1061–1062. doi: 10.1109/APUSNCURSINRSM.2019.8889182.

[50] D. Gabay, A. E. Yilmaz, A. Natan, and A. Boag, "Time-dependent response of carbon nanostructures," in *Proc. 2019 Int. Conf. Electromagn. Adv. Appl. (ICEAA)*, pp. 0886–0886. doi: 10.1109/ICEAA.2019.8879399.

[51] M. Ruggenthaler, J. Flick, C. Pellegrini, H. Appel, I. V. Tokatly, and A. Rubio, "Quantum-electrodynamical density-functional theory: Bridging quantum optics and electronic-structure theory," *Phys. Rev. A*, vol. 90, no. 1, p. 012508, 2014. doi: 10.1103/PhysRevA.90.012508.

[52] B. Fornberg, "Generation of finite difference formulas on arbitrarily spaced grids," *Math. Comput.*, vol. 51, no. 184, pp. 699–706, 1998. doi: 10.1090/S0025-5718-1988-0935077-0.

[53] A. E. Yilmaz, J. M. Jin, E. Michielssen, and D. S. Weile, "A fast Fourier transform accelerated marching-on-in-time algorithm for electromagnetic analysis," *Electromagnetics*, vol. 21, no. 3, pp. 181–197, 2001. doi: 10.1080/02726340151105166.

[54] A. A. Ergin, B. Shanker, and E. Michielssen, "The plane-wave time-domain algorithm for the fast analysis of transient wave phenomena," *IEEE Antennas Propag. Mag.*, vol. 41, no. 4, pp. 39–52, 1999. doi: 10.1109/74.789736.

[55] J. Meng, A. Boag, V. Lomakin, and E. Michielssen, "A multilevel Cartesian non-uniform grid time domain algorithm," *J. Computat. Phys.*, vol. 229, no. 22, pp. 8430–8444, 2010. doi: 10.1016/j.jcp.2010.07.026.

[56] S. Li, R. Chang, A. Boag, and V. Lomakin, "Fast electromagnetic integral-equation solvers on graphics processing units," *IEEE Antennas Propag. Mag.*, vol. 54, no. 5, pp. 71–87, 2012. doi: 10.1109/MAP.2012.6348120.

[57] D. Gabay, A. Boag, and A. Natan, "Optimizing kernel methods for Poisson integrals on a uniform grid," *Comp. Phys. Commun.*, vol. 215, pp. 1–6, June 2017. doi: 10.1016/j.cpc.2017.01.016.

[58] G. Kaur and A. E. Yilmaz, "Accuracy-efficiency tradeoff of temporal basis functions for time-marching solvers," *Microw. Opt. Technol. Lett.*, vol. 53, no. 6, pp. 1343–1348, 2011. doi: 10.1002/mop.25960.

[59] J. W. Eastwood and D. R. K. Brownrigg, "Remarks on the solution of Poisson's equation for isolated systems," *J. Computat. Phys.*, vol. 32, no. 1, pp. 24–38, 1979. doi: 10.1016/0021-9991(79)90139-6.